

Direct route from bio-ethanol to pure hydrogen through autothermal reforming in a membrane reactor: experimental demonstration, reactor modelling and design

V. Spallina^{a,c) 1}, G. Maturro^{a)}, C. Ruocco^{b)}, E. Meloni^{b)}, V. Palma^{b)}, E. Fernandez^{c)}, Jon Melendez^{c,d)}, A. Pacheco Tanaka^{c)}, J.L. Viviente Sole^{c)}, M. van Sint Annaland^{a)}, F. Gallucci^{a)}

a) Group of Chemical Process Intensification, Department of Chemical Engineering and Chemistry, Eindhoven University of Technology, Eindhoven, The Netherlands

b) Group of Processes and Catalysis for Energy and Environment depollution, Industrial Engineering Department, University of Salerno, Fisciano, Italy

c) Group of Membrane Technology, Energy and Environment Division, Tecnalia, San Sebastián-Donostia, Spain

d) Chemical Engineering and Environmental Department, University of the Basque Country UPV/EHU, Bilbao, Spain

Abstract

This work reports the integration of thin (~3-4 μm thick) Pd-based membranes for H_2 separation in a fluidized bed catalytic reactor for ethanol auto-thermal reforming. The performance of a fluidized bed membrane reactor has been investigated from an experimental and numerical point of view. The demonstration of the technology has been carried out over 50 hours under reactive conditions using 5 thin Pd-based alumina-supported membranes and a 3wt%Pt-10wt%Ni catalyst deposited on a mixed $\text{CeO}_2/\text{SiO}_2$ support. The results have confirmed the feasibility of the concept, in particular the capacity to reach a hydrogen recovery factor up to 70%, while the operation at different fluidization regimes, oxygen-to-ethanol and steam-to-ethanol ratios, feed pressures and reactor temperatures have been studied. The most critical part of the system is the sealing of the membranes, where most of the gas leakage was detected. A fluidized bed membrane reactor model for ethanol reforming has been developed and validated with the obtained experimental results. The model has been subsequently used to design a small reactor unit for domestic use, showing that 0.45 m^2 membrane area is needed to produce the amount of H_2 required for a 5 kW_e PEM fuel-cell based micro-CHP system.

¹ Corresponding Authors: v.spallina@tue.nl; f.gallucci@tue.nl

Keywords: ethanol reforming, palladium membranes, membrane reactor, hydrogen production, experimental demonstration, modelling

Introduction

H₂ represents an important product for the chemical industry [1], and its demand is constantly increasing, also due to its potential use as automotive fuel and energy carrier [2]. Nowadays, fossil fuels (and mostly natural gas) are used for the production of more than 95% of the global H₂. Currently, H₂ is almost entirely used as feedstock within the refining and chemical industries to convert raw materials into higher value chemicals (e.g. NH₃, CH₃OH) or refinery hydro-treating processes [3]. In addition, H₂ represents the most important energy carrier for the future and can play an important role in reducing the anthropogenic greenhouse gas emissions. Recently, fuel cells have been developed and launched to the market and a lot of research is ongoing to investigate and develop the technologies for the transition towards H₂ [4]. Among the various renewable feedstock alternatives, ethanol (EtOH) is considered as an attractive feedstock due to its relatively high hydrogen content, abundant availability, non-toxicity, storage or handling ease and safety [5–7]. Moreover, the ethanol can be produced renewably by biomass sources (agricultural wastes, forestry residuals or organic municipal wastes, etc.), also called bio-ethanol, and is mixed with water (about 15% on weight basis of EtOH [8]). The ethanol-to-hydrogen conversion is normally attained by ethanol reforming reactions that can be classified in: i) steam reforming (ESR) and ii) auto-thermal reforming (EAR) in the presence of an oxidant (air or oxygen).

The reaction pathways for ethanol reforming include several possible reactions which are influenced by the catalyst and the operating conditions used in the system [5,9,10]. Different supported/unsupported catalysts have been proposed in the literature for the ESR reaction which have been summarized in a recent review from Hou et al. [9], where both noble metal catalysts (Rh, Ru, Pt, Pd) operated in the range of 650-750 °C with a steam-to-ethanol ratio (H₂O/EtOH) of 1-3 (and also O₂ co-feeding) and transition metals (especially Ni and Co) operated at a lower temperature (350-650 °C) with a higher H₂O/EtOH ratio (up to 10 on a molar basis) have been considered. However, the addition of small quantities of noble metals to transition metals-based catalysts was shown to improve the ethanol conversion and H₂ yield even at low temperatures and/or steam-to-carbon ratios [11]. As support material, alumina (Al₂O₃) has been widely studied because of its strong thermal and mechanical stability, despite the fact that it may allow the formation of C₂H₄ which is a precursor for coke formation. In general, supports such as CeO₂ and mixed oxides systems have shown to be highly favourable in terms of EtOH conversion and H₂ selectivity reducing the sintering effect

because of metal dispersion through the support [11,12]. As a result, the application of the high surface area of a CeO₂/SiO₂ mixed system has shown improved catalytic stability with respect to SiO₂ free samples [13].

H₂ production from ethanol is normally carried out via multiple steps of conversion and separation processes [10,14]. The reforming is carried out at 750-800 °C, where the ethanol is decomposed in other gaseous species (CH₄, CO, H₂) as indicated in Equation (1), making the conversion of ethanol into H₂ thermodynamically limited. In the ethanol auto-thermal reforming (EAR), the presence of oxygen reduces the H₂ selectivity, however, no external furnace is required to supply the required heat of reaction for the highly endothermic ESR. Due to the thermodynamic equilibria, large quantities of CO are produced. The main reactions occurring in the EAR reactor are:



In the complete process, the H₂ yield can be enhanced by employing additional water-gas-shift (WGS) reactors, producing H₂ and CO₂ while reducing the CO content below 1-0.5 vol.%. In some processes, the presence of CO in the H₂-rich stream acts as a poison for the materials of the downstream units (e.g. fuel cells, NH₃ synthesis, etc.). In these cases, a further purification step is required to obtain high purity H₂, and usually a methanation reactor is considered to further decrease the CO content to below 10 ppm converting CO into CH₄ [15]. Alternatively, pressure swing absorption (PSA), cryogenic distillation, or membrane technology can be used to produce high purity H₂ (>99.99%).

The overall H₂ yield of ethanol reforming is usually about 4.3 mol_{H₂}/mol_{E₁O_H} [14]. However, in case pure H₂ is required, the application of PSA (with an H₂ separation factor of about 80%) leads to an overall efficiency (based on the LHV) of 65% (<3.5 mol_{H₂}/mol_{E₁O_H}).

Recently, several studies have been devoted to the integration of ethanol reforming and H₂ separation using Pd-based membranes [16–18]. Pd-based membranes are inorganic membranes in which H₂ permeates selectively from the feed/retentate to the permeate side. Pd-based membranes are normally alloyed with other metals (Cu, Ag, Au, etc.) to enhance the performance and the tolerance to embrittlement and poisonous gases (i.e. H₂S) and generally are thin films supported on metallic or ceramic supports in order to enhance the mechanical resistance while achieving high fluxes [19–23]. Membrane reactors represent a

convenient solution to integrate reaction and separation in a single process with several advantages: i) the chemical equilibrium is shifted towards the products and therefore no other conversion units are required, ii) the cost of materials can be reduced by operating at lower temperatures, iii) the H₂ separation and purification is carried out in-situ, iv) the membrane reactor can be integrated in small and medium scale plant. So far, several different processes have been proposed to integrate Pd membranes for H₂ production differing in reactor configuration and/or plant design [21,24,25]. Also membrane reactors for EtOH reforming have been extensively studied. Borgognoni et al. [18] have tested a CH₄/EtOH co-feeding unit in which the reforming is carried out at 750 °C and the H₂ separation is carried out in a downstream membrane separator in which the 70% of the total amount of produced H₂ was recovered at 500 kPa. Basile et al. [16] have tested a packed bed membrane reactor using different H₂O/EtOH ratios (ranging from 3 to 9) at 1.3 bar in the range of 300-400 °C and a Ru-based catalyst supported on Al₂O₃; in this work the total hydrogen recovery factor (HRF) was between 10%-56% depending on the temperature and the H₂O/EtOH ratio used. Gallucci et al. [17] have proposed a fluidized bed membrane reactor for ethanol reforming in which part of the H₂ is consumed in a dedicated membrane which uses air as sweep gas, so that the combustion provides the heat of reaction for the ethanol reforming while CO₂ capture was integrated: about 15% of the total membrane area is required for combustion to achieve autothermal operation and the maximum CO₂ selectivity was reached at 700 °C due to the higher permeation rate of the membrane at higher temperatures. The use of a fluidized bed reactor improves the temperature control of the system avoiding the possible formation of hotspots, as well as the presence of low temperature zones which may damage the Pd-based membranes because of embrittlement. De Falco [26] has investigated an ethanol membrane reformer integrated with a polymeric electrolyte membrane fuel cell for automotive vehicles, delivering an optimized design of a 0.2 m³ reactor with 4 membranes (0.285 m² of membrane area) operated at 400 °C for the production of 64 NL·min⁻¹ of H₂ to work in a PEM fuel cell of 4 kW_e. Foresti and Manzolini [14] have performed a thermodynamic analysis for a micro combined heat and power generation unit (μCHP) in which a fluidized bed membrane reactor is used for ethanol auto-thermal reforming and pure H₂ separation integrated with a 5 kW_e PEM fuel cell to generate heat and electricity for domestic off-grid applications. In their work, the authors have compared different membrane reactor configurations (with and without sweep gas) at 500-550 °C varying the pressure (6-16 bar) and the composition (H₂O/EtOH from 3 to 4.2) resulting in an optimal system performance (higher than 40% of electrical efficiency compared to 33.1% of the conventional case) at 12 bar and a H₂O/EtOH ratio equal to 3.6 and 0.4 m² of membrane area. In case of H₂ separation without sweep gas, the optimal performance that could be achieved at 6 bar and 0.3 bar at the permeate side required 0.3 m² membrane area (40.3% based on Ethanol lower heating value). Recently, Arratibel et al. [27]

have summarized the operating conditions and performance of different methane and ethanol reforming membrane reactor for pure H₂ production that have been tested and presented.

In the present paper, a fluidized bed membrane reactor (FBMR) has been tested for ESR and EAR and evaluated from an experimental and numerical point of view. The catalyst material used is 3wt%Pt-10wt%Ni deposited onto a mixed CeO₂/SiO₂ support to increase the stability of the catalyst as presented in a previous work [12]. Five ultra-thin ceramic-supported Pd-Ag membranes (4 μm thickness) of 120-160 mm length and 10 mm of external diameter have been sealed and integrated in a lab-scale fluidized bed (previously used to demonstrate a WGS membrane reactor [24]) and tested under reactive conditions. The proof-of-concept has been achieved for different operating conditions. A two-phase phenomenological model for the fluidized bed reactor has been validated with the experimental results and subsequently used for the design of a commercial scale unit.

Description of the technology

The schematic representation of a fluidized bed membrane reactor is shown in [Figure 1](#). The inlet gases, EtOH/H₂O/air, are fed to the bottom part of the reactor through a 40 micron porous plate distributor. All the EtOH is partly oxidized with O₂ and decomposed into other gases (reaction (1)), while the produced CH₄ and CO start to react with H₂O (reactions (2-4)). The supported Pd-Ag membrane tubes are immersed inside the catalyst bed to extract the hydrogen from the reaction zone and enhance the methane reforming and water gas shift reactions. The pressure drop over the bed is negligible, while mass and heat transfer coefficients are higher due to the vigorous solids mixing resulting in a virtually uniform temperature throughout the reactor.

The presence of the membranes can improve the bubble-to-emulsion mass transfer rate, since the membranes act as internals in the granular suspension promoting bubble breakage [28]. Due to the gas extraction through the membranes, the solids circulation pattern may be modified compared to the conventional fluidized bed reactor, since densified zones may be formed close to the membranes [29,30].

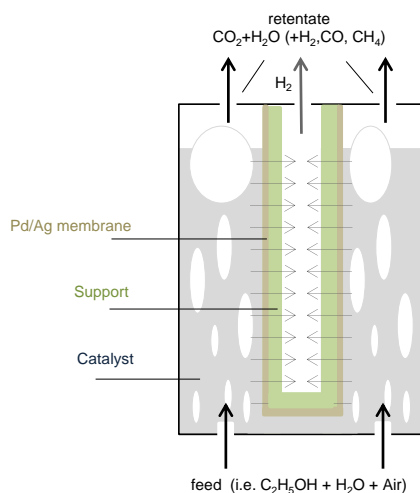


Figure 1: Schematic layout of a fluidized bed membrane reactor

The integration of catalyst and membranes has been carried out at two different scales: in the first part, a single tube membrane reactor has been used to carry out permeation tests using different reactor layouts (empty, fluidized and packed bed configurations) to verify the validity of the kinetic model proposed in Ruocco et al. [12]. Subsequently, 5 membranes have been sealed and used in a larger prototype, which has been operated close to industrial operating conditions.

Catalyst preparation

The $\text{CeO}_2/\text{SiO}_2$ support material was prepared by adding calcined (at $600\text{ }^\circ\text{C}$ for 3 h, heating rate of $10\text{ }^\circ\text{C}\cdot\text{min}^{-1}$) silica gel (particle size distribution $150\text{-}250\text{ }\mu\text{m}$, supplied by Sigma-Aldrich) to an aqueous solution of $\text{Ce}(\text{NO}_3)_3\cdot 6\text{H}_2\text{O}$ (Strem Chemicals). The $\text{CeO}_2/\text{SiO}_2$ weight ratio, previously optimised [13], was fixed at 30%. Impregnation was carried out at $80\text{ }^\circ\text{C}$ for 2 h on a heating and stirring plate. Then, the support was filtered by means of a Buchner funnel, dried overnight at $120\text{ }^\circ\text{C}$ and calcined as reported above for the bare silica. Ni (10wt%) and Pt (3wt%) metal loadings refer to the total ceria mass were sequentially added to the support, starting from $\text{Ni}(\text{NO}_3)_2\cdot 6\text{H}_2\text{O}$ and PtCl_4 (Strem Chemicals) as salt precursors, respectively.

BET specific surface areas and porosity of the support as well as the catalyst were determined from the absorption isotherms at 77 K, acquired by means of a ThermoScientific Surfer. Structural properties were characterized by powder X-ray diffraction (XRD) using a D-8 Advance Bruker WAXRD diffractometer under a $\text{CuK}\alpha$ radiation of 1.5406 \AA . XRD spectra allowed the calculation of average crystallite size by means of [Scherrer](#) equation. H_2

Temperature Programmed Reduction (TPR) measurements were carried out in situ in the laboratory apparatus previously described [13]. The temperature was increased to 600 °C (heating rate of 10 °C/min) and held for 1 h under 5%H₂ in N₂ (500 Ncm³·min⁻¹ of total flow rate). The support and catalysts were prepared and characterized (XRD and TPR analysis) in the Proceed laboratories of the University of Salerno.

Membrane preparation

Alumina asymmetric tubes with a 10 mm outside diameter were used as membrane supports. Pd-Ag thin layers were deposited onto the alumina tubes using the simultaneous (Pd and Ag) electroless plating technique reported in Pacheco Tanaka et al. [31]. After the plating step, the membrane layers were annealed at 550 °C with a H₂-N₂ gas mixture. The final membranes are approximately 140-230 mm in length and with a Pd-Ag thickness of around 3-4 μm (Figure 2).

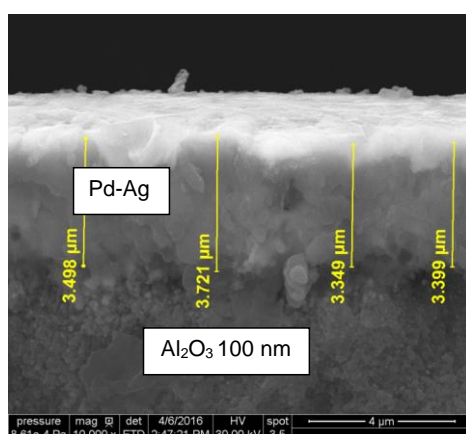


Figure 2: Cross-section SEM image of a Pd-Ag membrane layer deposited onto an Al₂O₃ asymmetric porous tube (100 nm pore size, 10/4 mm OD/ID).

Reactor design and test rig

Two different reactors have been used in this work. The first reactor is a single tube membrane reactor (Figure 3a) which has been used for the permeation tests and the validation of the kinetic modelling by feeding a mixture of CH₄, CO and H₂ and H₂O under fluidization conditions. The membrane (named E275) is 5.5 cm in length and has an external diameter of 10 mm (Figure 3b). The sealing method has been proposed by Chen et al. [32] in which graphite ferrules, instead of metal ferrules are used. The same method has been successfully

used for a long-term test under reactive conditions [19,24,33]. The reactor is placed in an electrically heated oven in order to have a constant temperature along the entire reactor. A second membrane (E273) of 10.4 mm (ID) and 109.8 cm length was also used for the permeation test using respectively the empty bed, packed bed and fluidized bed configurations.

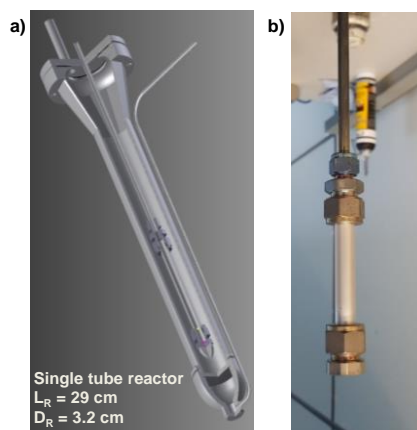


Figure 3: a) Schematic layout of the single tube membrane reactor; b) Pd-Ag membrane used for the experiments.

The second reactor has an inner diameter of 10 cm and a length of 1 m is located inside an electric heated jacket and details are shown in Figure 4 and Figure 5. This experimental set-up allows performing reactive permeation experiments with a maximum of five membranes. There are three thermocouples, and two pressure sensors distributed over the reactor height. A vacuum pump is located at the permeate side, in order to separate H_2 at 10-30 mbar. The system further includes feed connections to pure gas components as O_2 , H_2 , N_2 , CO , CO_2 , CH_4 and pressurized air, as well as liquid tanks containing H_2O and $EtOH$. Both $EtOH$ and water are connected to a CEM (Controlled Evaporator Mixer) where both components can be evaporated before feeding to the reactor. All the tubes connected to the reactor inlet are traced, as well as the tubes used for the retentate, to maintain the temperature well above the boiling point of water and ethanol. In order to measure the $EtOH$ content in the retentate stream, an *Agilent Technologies* Cary 630 FTIR with CaF_2 windows was used together with a *RED-SHIFT* gas sampling system. The FTIR was calibrated prior to the experiments using the classical Lambert-Beer law in typical adsorption spectra for the gases CO_2 , CH_4 and $EtOH$. After that, the retentate passes through a cooler where the water and ethanol (if present) are condensed and separated in a flash column. The retentate is connected to a Sick® analyzer to measure the retentate composition (dry basis). A similar analyzer is also connected to the

permeate side, which is able to measure hydrogen concentrations in the range of 0-100% and CO_x concentrations on a ppm level. The flow rate at the permeate side is measured with a Horiba film flow meter. The membranes can also be assessed individually, by closing valves manually which are placed on top of the reactor.

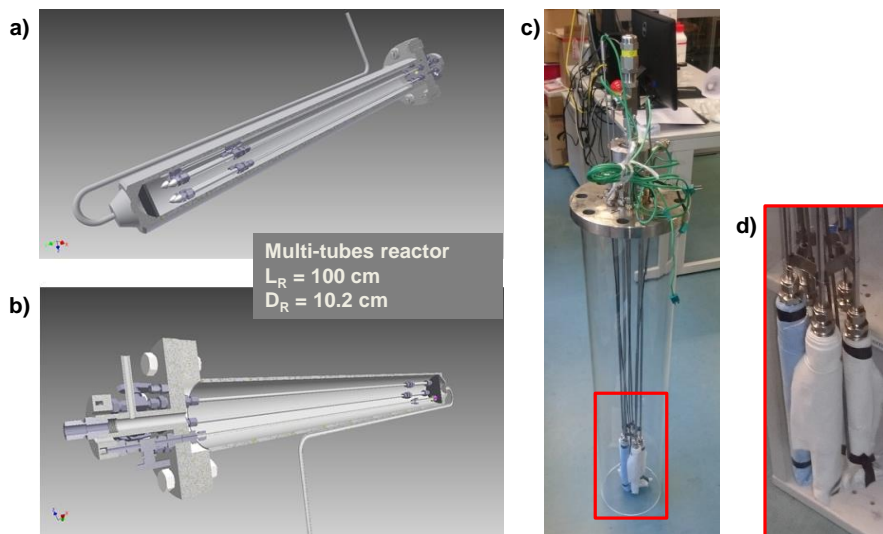
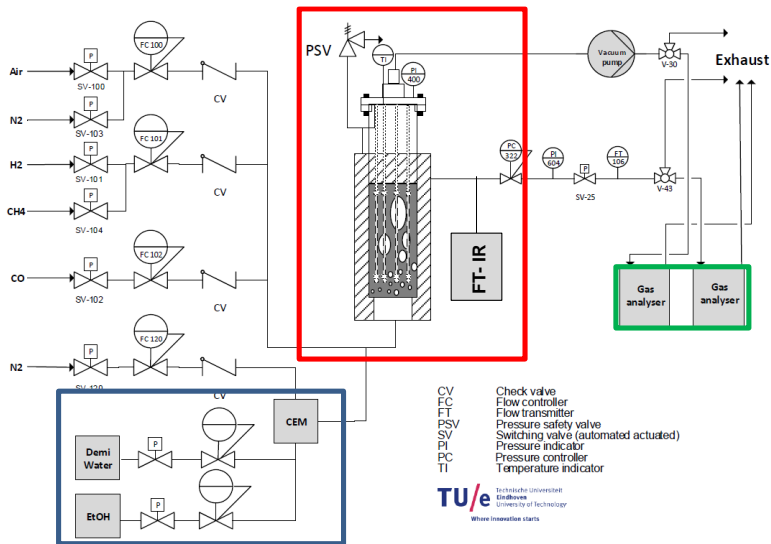


Figure 4: a) and b) Schematic layout of the multi-tubular membrane reactor; c) membrane tube bank arrangement prior to placement inside the reactor; d) zoomed in picture of the membrane arrangement.



a)



b)



c)



d)

Figure 5: a) P&ID of the setup used for the multi-tubular experiments; b) Vessels of EtOH and H₂O used for the experiments, c) Electric oven and reactor; d) Gas analysers for the permeate (left) and retentate (right) streams.

Reactor model

The phenomenological two-phase model for the membrane-assisted fluidized bed reactor is depicted in [Figure 6](#). This model has been developed in the past years and used for different processes involving H₂/O₂ membrane reactors [34,35]. Both emulsion and bubble phases are considered as a cascade of a number of continuous stirred tank reactors (CSTRs) and the size of the CSTRs is directly related to the extent of gas back-mixing in each phase. The model assumptions are as follows: i) the reactor consists of two phases, viz. bubble and emulsion

phases; ii) the gas through the emulsion phase is assumed completely mixed in each CSTR and at incipient fluidization conditions; iii) the bubble phase is considered to be in plug flow (and therefore several CSTR are used to properly account for it); iv) the reactions involved in the system occur only in the emulsion phase (i.e. the bubbles are assumed devoid of particles); v) the gas that permeates through the membrane is taken from both bubble and emulsion phases in a ratio according to their local phase fractions; note that the gas extracted from the emulsion phase is replaced by part of the gas transferred from the bubble phase in order to respect the minimum fluidization velocity; vi) the temperature is assumed constant along the entire bed.

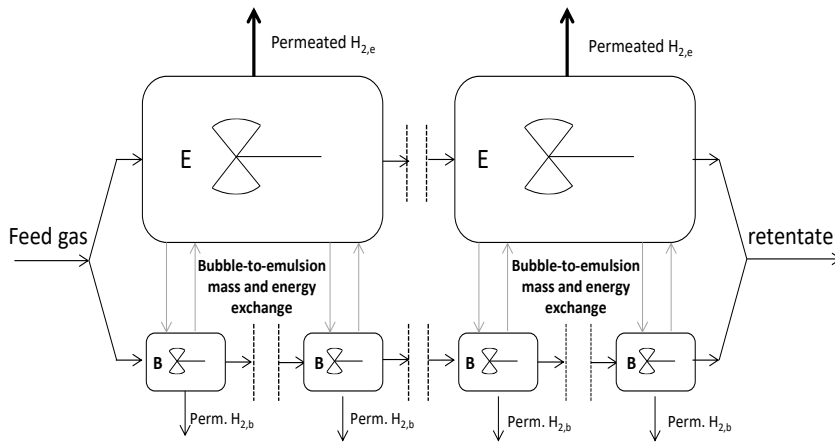


Figure 6: Schematic of the two-phase phenomenological model [17].

The overall component mass balance equations have been formulated accounting for the chemical reactions and the gas permeation in the source terms. More details on the material and energy balances and additional parameters for the membrane-assisted fluidized bed reactor model can be found in Gallucci et al. [17].

Table 1: Hydrodynamic parameters and mass transfer coefficients used in the model

Parameters	Equation	Ref.
Archimedes number	$Ar = d_p^3 \rho_g (\rho_p - \rho_g) g / \mu_g^2$	(5) [36]
Minimum fluidization velocity	$u_{mf} = (\mu_g / d_p \rho_g) \left(\sqrt{(27.2)^2 + 0.0408 Ar} - 27.2 \right)$	(6) [37]
Bed voidage at minimum fluidization velocity	$\epsilon_{mf} = 0.586 Ar^{-0.029} \left(\frac{\rho_g}{\rho_p} \right)^{0.021}$	(7) [37]
Velocity of rise of swarm of bubbles	$u_b = u_o - u_{mf} + u_{br}$	(8) [36]

Eliminato: 7

Eliminato: 8

Eliminato: 9

Eliminato: 10

Rising velocity of single bubble	$u_{br} = 0.711(g \cdot d_{b,avg})^{1/2}$	(9) [36]	Eliminato: 11
Emulsion velocity	$u_e = \frac{u_o - \delta \cdot u_b}{1 - \delta}$	(10) [36]	Eliminato: 12
Average bubble diameter	$d_{b,avg} = d_{b,max} - (d_{b,max} - d_{bo}) \exp\left(-\frac{0.3H}{D_T}\right)$	(11) [38]	Eliminato: 13
Initial bubble diameter	$d_{bo} = 0.376(u_o - u_{mf})^2$	(12) [35]	Eliminato: 14
Bubble phase fraction	$\delta_{bn} = \frac{u_b^s}{u_b}$	(13) [35]	Eliminato: 15
Emulsion phase fraction	$\delta_{en} = 1 - \delta_{bn}$	(14) [35]	Eliminato: 16
Maximum superficial bubble gas velocity	$u_{b,max}^s = u_o - u_{mf}$	(15) [35]	Eliminato: 17
Initial superficial bubble gas velocity	$u_{b,o}^s = u_{br,o} \delta_{bo}$ where $\delta_{bo} = (1 - H_{mf} / H_f)$	(16) [35]	Eliminato: 18
Height of bed at minimum fluidization velocity	$H_{mf} = H_s \frac{1 - \varepsilon_s}{1 - \varepsilon_{mf}}$	(17) [38]	Eliminato: 19
	$H_f = H_{mf} \frac{C_1}{C_1 - C_2}$	(18)	Eliminato: 20
	where,		
Height of bed expansion	$C_1 = 1 - \frac{u_{b,o}}{u_{b,avg}} \exp\left(-\frac{0.275}{D_T}\right)$	(19) [35]	Eliminato: 21
	$C_2 = \frac{u_b^s}{u_{b,avg}} \left[1 - \exp\left(-\frac{0.275}{D_T}\right)\right]$	(20)	Eliminato: 22
Average bubble rise velocity	$u_{b,avg} = u_o - u_{mf} + u_{br}$	(21) [35]	Eliminato: 23
	$K_{bc} = 4.5 \left(\frac{u_{mf}}{d_p}\right) + 5.85 \left(\frac{D_g^{1/2} g^{1/4}}{d_b^{5/4}}\right)$	(22)	Eliminato: 24
Gas exchange coefficient	$K_{ce} = 6.77 \left(\frac{D_g \varepsilon_{mf} u_b}{d_b^3}\right)^{1/2}$	(23) [35]	Eliminato: 25
	$\frac{1}{K_{be}} = \frac{1}{K_{bc}} + \frac{1}{K_{ce}}$	(24)	Eliminato: 26

The kinetic model is based on the results presented by Ruocco et al. [12], which have been validated against experimental results and compared with other models available in the literature:

- $C_2H_5OH + 3.5\alpha O_2 \rightarrow (1 - \alpha)C_2H_5OH + 2\alpha CO_2 + 3\alpha H_2O$: the reaction is completely shifted toward the products until the oxygen is completely consumed;
- $(1 - \alpha)C_2H_5OH \rightarrow (1 - \alpha)CH_4 + (1 - \alpha)H_2 + (1 - \alpha)CO$: full conversion is assumed with an infinite reaction rate;
- $CH_4 + H_2O \leftrightarrow CO + 3H_2$: the reaction rate of the steam methane reforming (SMR) reaction has been determined experimentally;

- $\text{CO} + \text{H}_2\text{O} \leftrightarrow \text{CO}_2 + \text{H}_2$: water gas shift reaction (WGS) has been assumed at chemical equilibrium.

An empirical power-law expression is used to describe the kinetics of SMR. The power-law expression generally used for the SMR is:

$$R_{SMR} = k_{SMR} (P_{CH_4}^a P_{H_2O}^b P_{CO}^c P_{H_2}^d) (1 - \beta) \quad (25)$$

where $\beta = \left(\frac{1}{K_{eq}^{SMR}} \frac{P_{H_2}^3 P_{CO}}{P_{CH_4} P_{H_2O}} \right)$ $a = 0.96$
 $b = 0.28$
 $c = d = 0$

And $K_{eq}^{SMR} = \exp\left(-\frac{\Delta G^{SMR}}{RT}\right)$

$$k_{SMR} = k_{0,SMR} \exp\left(-\frac{E_{act,SMR}}{RT}\right) \quad \begin{matrix} E_{act,SMR} = 72.8 \text{ kJ/mol} \\ k_{0,SMR} = 8.02 \times 10^2 \text{ mol}/(\text{kg}_{cat}\text{s Pa}^{a+b+c+d}) \end{matrix} \quad (26)$$

The H_2 permeation rate has been described ($\text{mol}_{\text{H}_2}/\text{m}^2$) with Sieverts' law:

$$J_{H_2} = P_{H_2,0} \exp\left(-\frac{E_{H_2,p}}{RT}\right) (P_{H_2,r}^{0.5} - P_{H_2,p}^{0.5}) \quad \begin{matrix} E_{H_2,p} = 4.57 \text{ kJ/mol} \\ P_{H_2,p} = 1.14 \times 10^{-4} \text{ mol}/(\text{s m}^2 \text{ Pa}^{0.5}) \end{matrix} \quad (27)$$

The membrane permeation rate is discussed in more detail the next section.

Results

Catalyst characterization

The specific surface area, average pore diameter (D_p) and the pore volume (V_p) of the support and the final catalyst are shown in [Table 2](#). The N_2 adsorption-desorption isotherm curves at 77 K ([Figure 7](#), (a) and (b)), according to the IUPAC classification, belong to type IV, typical of mesoporous structures [39]. The mesoporous structure of the CeO_2 - SiO_2 support as well as its specific area was unaffected by the deposition of the active species. In both cases a broad hysteresis loop was observed, which is typical of mesoporous solids; however, the presence of micropores (pores with sizes smaller than 2 nm) cannot be excluded [40]. The XRD patterns of the support and the catalysts are shown in [Figure 7](#), (c). The broad peak around 23° can be attributed to amorphous SiO_2 while the diffraction peak at 43.2° , observed in the spectrum of the Pt-Ni/ CeO_2 - SiO_2 sample, is related to the NiO crystalline phase [41]. Diffraction lines of the CeO_2 fluorite-type structure are also visible in both patterns. As a result of the high surface area of the silica support ($400 \text{ m}^2\cdot\text{g}^{-1}$), very low dimensions for ceria and nickel oxides crystallites were recorded (equal to 82 and 85 \AA respectively). Similarly to the results shown

Eliminato: 5

Eliminato: 6

Eliminato: Table 2

Formattato: Tipo di carattere: Grassetto

Formattato: Tipo di carattere: Grassetto

Eliminato: Figure 6

Eliminato: ordered

Formattato: Tipo di carattere: Grassetto

Eliminato: Figure 7

in [Table 2](#), the deposition of the active species had no effect on the ceria crystallite sizes (78 vs 82 Å).

Table 2: Specific surface area (BET), porous volume (V_p) and ceria crystallite sizes (D_p) of the fresh CeO_2 - SiO_2 and Pt-Ni/ CeO_2 / SiO_2 samples.

Sample	BET ($\text{m}^2\cdot\text{g}^{-1}$)	D_p (nm)	V_p ($\text{cm}^3\cdot\text{g}^{-1}$)
$\text{CeO}_2/\text{SiO}_2$	254	2.82	0.802
Pt-Ni/ $\text{CeO}_2/\text{SiO}_2$	255	2.86	0.807

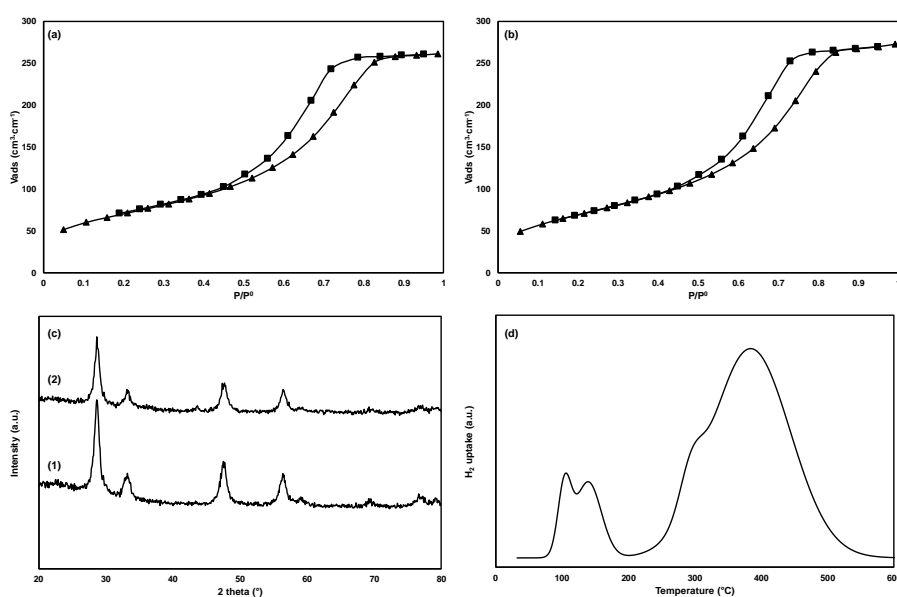


Figure 7. N_2 adsorption (square)-desorption (triangle) isotherms at 77 K for $\text{CeO}_2/\text{SiO}_2$ (a) and Pt-Ni/ $\text{CeO}_2/\text{SiO}_2$ (b), XRD spectra of the support (1) and the final catalyst (2) (c), TPR profile after deconvolution for the Pt-Ni/ $\text{CeO}_2/\text{SiO}_2$ sample (d).

The catalyst was also characterized by H_2 -TPR ([Figure 7, \(d\)](#)) in order to investigate the Ni as well as Pt interactions with the $\text{CeO}_2/\text{SiO}_2$ support. Two zones were observed, at 70-200 $^\circ\text{C}$ and 200-600 $^\circ\text{C}$, related to the noble and the non-noble metal reduction respectively [42]. Both low and high temperature reduction zones can be deconvoluted into two peaks, which proves the presence of oxides particles with different interactions with the support. In the case of NiO, for example, the peak observed at 294 $^\circ\text{C}$ can be ascribed to the reduction of bulk particles, having weak interaction with the support, whereas the peak at 384 $^\circ\text{C}$ is attributed to nickel oxide particles in intimate contact with $\text{CeO}_2/\text{SiO}_2$. The total hydrogen consumption ($3802 \mu\text{mol}_{\text{H}_2}\cdot\text{g}_{\text{cat}}^{-1}$) is almost twice the expected one, [which suggests that active species deposition on the catalyst may improve the bulk-phase oxygen reduction of \$\text{CeO}_2\$, commonly negligible](#)

Formattato: Tipo di carattere: Grassetto

Eliminato: Figure 7

below 600°C [43]. This effect is enhanced by the better Ni reducibility observed after Pt addition, related to spillover phenomena and commonly reported in the literature, which also resulted in lower reduction temperatures for nickel oxide phase [44]. On the other hand, the low dimension of ceria crystallites as well as the CeO₂-SiO₂ interactions may further improve ceria surface oxygen reducibility [43].

Membrane Permeation

The permeation tests were carried out with the same membrane at the same operating conditions while the reactor configurations were modified. After sealing the membrane (using a torque wrench with a momentum >10 Nm), the membrane leakages are detected by immersing the membrane inside ethanol and feeding He internally to the membrane (with a ΔP of 1 bar). The He leakage is totally concentrated in the sealing part and corresponds to 0.036 ml·min⁻¹. After that, the membrane was located inside the reactor and heated up to 400 °C in a N₂ environment. During the heating, air was shortly flowing inside the reactor in order to clean the membrane surface from any unwanted species. When the system is at 400 °C, a mixture of H₂/N₂ is used to activate the membrane. Membrane activation is reached when the H₂ permeation is no longer increasing after two consecutive flux measurements.

The first tests have been carried out using the E273 membrane. The membrane permeation rate was measured at 400 °C with three different configurations and the comparison is shown in [Figure 8](#). In the empty configuration (represented by a circle in [Figure 8](#)), no solids are placed inside the reactor and the permeation tests are carried out using different H₂/N₂ compositions (100/0, 80/20, 60/40, 50/50), where 4 NI·min⁻¹ of H₂ is fed to the system while the amount of N₂ is properly adjusted. The total pressure at the feed/retentate side is varied from 1.5 to 4 bar, while the permeate side pressure is kept at 1 bar. Due to limitations in the total pressure, when decreasing the H₂ content fewer measurements were possible in order to guarantee a positive H₂ permeation driving force from the retentate to the permeate side. After the test without solids inside the reactor, two more tests have been carried out. Firstly the reactor has been filled with 95 g of CeO₂/SiO₂ with particle size in the range of 150 - 250 μm, so that permeation tests could be carried out under fluidization conditions (these results are marked with triangles in [Figure 8](#)). Finally, the reactor has been completely filled with inert material with a particle size of 1-1.5 mm to have the membrane operated in a packed bed configuration (square markers in [Figure 8](#)).

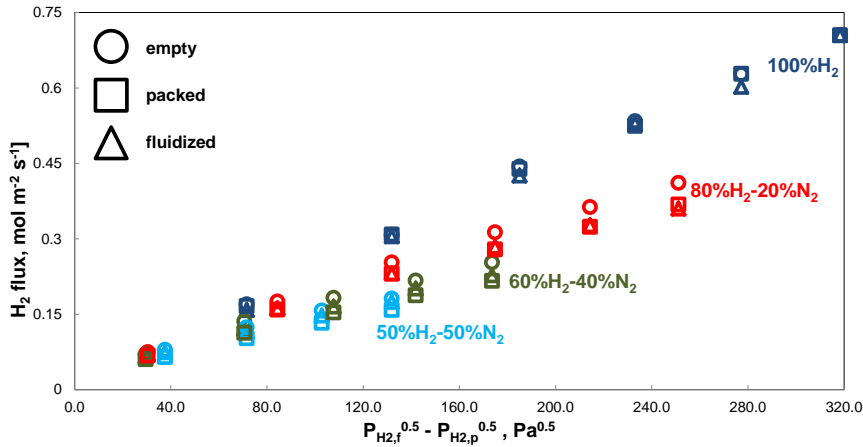


Figure 8: H₂ flux as a function of the permeation driving force for different H₂-N₂ compositions and configurations at 400°C with the E273 membrane.

Two main conclusions can be derived from the analysis of these results. The first conclusion is a confirmation that the extent of concentration polarization is considerable. The slope of the curve - which corresponds to the membrane permeance according to equation (27) - decreases by a 53% (respectively $2.18 \cdot 10^{-3} \text{ mol m}^{-2} \text{ s}^{-1} \text{ Pa}^{-0.5}$ and $1.03 \cdot 10^{-3} \text{ mol m}^{-2} \text{ s}^{-1} \text{ Pa}^{-0.5}$) when comparing the gas feed compositions of 100% H₂ and 50/50 H₂/N₂. These results are also confirmed by several other works available in the literature [44–48], specifically in the presence of high flux membrane as is the case of ultra-thin ($\sim 1 \text{ }\mu\text{m}$ thickness) Pd-based membranes. The same trend is also shown in case of fluidized and packed bed configurations. Remarkably, only a negligible improvement (+6-8%) is observed when using the fluidized bed configuration with respect to the packed bed configuration. Helmi et al. [24] have demonstrated that the H₂ permeation in a membrane reactor is enhanced when employing a fluidized bed configuration due to the increased radial dispersion; they have carried out an experimental campaign operating the system at $3 < u/u_{mf} < 5$ by adjusting the flow rate according to the fluidization regime adopted. In this part of the study, the gas flow rate was kept constant resulting in a different fluidization regime. Specifically, when comparing the empty bed with the packed bed configuration, the radial diffusion/dispersion can be estimated at respectively $3.13 \cdot 10^{-4} \text{ m}^2 \text{ s}^{-1}$ and $1.22 \cdot 10^{-4} \text{ m}^2 \text{ s}^{-1}$ (according to the Tsotsas and Schlünder [49] correlation) which explains the slightly lower permeation rate obtained with the packed bed configuration. In case of the fluidized bed reactor, when the same inlet flow rate is used, the u/u_{mf} is about 44 ($u_{mf} = 0.014 \text{ m s}^{-1}$), therefore the gas velocity is almost equal to the terminal velocity u_t estimated at 0.91 m s^{-1} . This implies operation in the slugging regime with the presence of

large bubbles surrounding the membrane, which reduces the radial dispersion without any advantages in the permeation rate compared to the empty bed.

Prototype reactor test

The multi-tubular membrane reactor has been tested in continuous operation. Before starting the permeation test under reactive conditions, the 5 membranes have been checked separately. The results in terms of H₂ permeance² and H₂/N₂ ideal perm-selectivity are shown in Table 3, and clearly indicate that the current permselectivity is insufficient to reach the H₂ purity of 99.99% as required for PEM fuel cells applications unless a downstream methanation reactor is used to decrease the CO level in the permeate to values below 10 ppm. However, it should be noted that most of the leakages originates from the sealing of the membrane, thus a stronger support material as well as specific Swagelok connectors could be used to reduce the leakages and improve the permselectivity.

The 5 membranes have been on stream under high temperature and fluidization conditions for three weeks in which reactive experiments (using EtOH) were carried out for overall 50 hours. During the remaining time a mixture of N₂ and H₂ was used to keep the bed under fluidization conditions.

Table 3: Membrane performance used for the prototype before reactive tests

Membranes	Name	Length mm	Area cm ²	H ₂ Permeance (pure gas) mol s ⁻¹ m ⁻² Pa ^{-0.5}	H ₂ /N ₂ Selectivity ² P _{H2} /P _{N2}
Membr_1	FL-4	146.6	47.85	1.46E-03	893
Membr_2	FL-5	148.4	48.44	8.58E-04	1319
Membr_3	FL-6	175	57.12	8.08E-04	590
Membr_4	FL-7	187	61.04	7.36E-04	2836
Membr_5	FL-8	153.5	50.10	8.96E-04	803
total area			264.56		

The operating temperature of the reactor has been varied in the range of 450-550 °C; the pressure at the feed/retentate side has been varied from 2-4 bar; the gas flow rate has been adjusted in order to always keep a u/u_{mf} equal to 3. As reference case, the O₂/EtOH ratio has been set at 0.4 (on a molar basis) and the H₂O/EtOH at 6. The amount of EtOH fed to the system has been varied between 100 and 250 Nml·min⁻¹ to ensure a constant gas composition and fluidization regime.

For all the tests, the EtOH conversion at the reactor outlet was above 99.9%, demonstrating that the catalyst was highly active with respect to ESR and EAR reactions and the system is

² The H₂/N₂ ideal perm-selectivity is the average ratio of the H₂ and N₂ permeance values at 450 °C in the range of 2.5-4.5 bar.

at its thermodynamic equilibrium, when accounting for the hydrogen that has been extracted from the system.

From the analysis of the composition at the retentate side (shown in Figure 9), the following conclusions can be derived:

- The CH₄ conversion increases when increasing both the temperature or pressure, while the CO content increases at higher temperatures, which confirms that i) the amount of catalyst and the residence time in the reactor are sufficiently high to avoid any kinetic limitation in the conversion of the reactants and ii) the higher the amount of permeated H₂, the more the equilibrium is shifted towards the products. Specifically, at 550 °C the CH₄ fraction is only 0.1-0.3 vol%.
- At increased pressure the amount of H₂ that permeates through the membrane increases due to the higher driving force between the retentate and the permeate side (where 0.03 bar(a) is considered when using the vacuum pump).
- The CO, CO₂, and H₂ concentrations in the permeate side were frequently measured during experiments. The permeated CO and CO₂ concentrations were in the range of 100–300 ppm, whereas the hydrogen concentration was measured constantly at values above 98%, where the remaining 2% is expected to be N₂ for all the experiments.
- The error in the carbon balance is always <5% demonstrating that all the EtOH is converted into CH₄/CO/CO₂ and carbon deposition is not occurring at the investigated conditions.
- With respect to the general definition of the Hydrogen Recovery Factor, HRF³, the experiments have shown that a higher HRF is reached by increasing the temperature and decreasing the pressure. At a higher pressure the increase in the amount of permeated H₂ is less than the increase in the amount of EtOH fed at the inlet (to achieve the required u/u_m), while at a higher temperature both the increase in the permeation rate and the CH₄ conversion increase the amount of separated H₂. Overall the measured HRF is ranging between 27.5% (@450 °C and 4 bar) to 43% (@ 550°C and 2 bar).

$$^3 HRF = \frac{(H_{2, \text{permeated}})}{(6C_2H_5OH - 2O_2)}$$

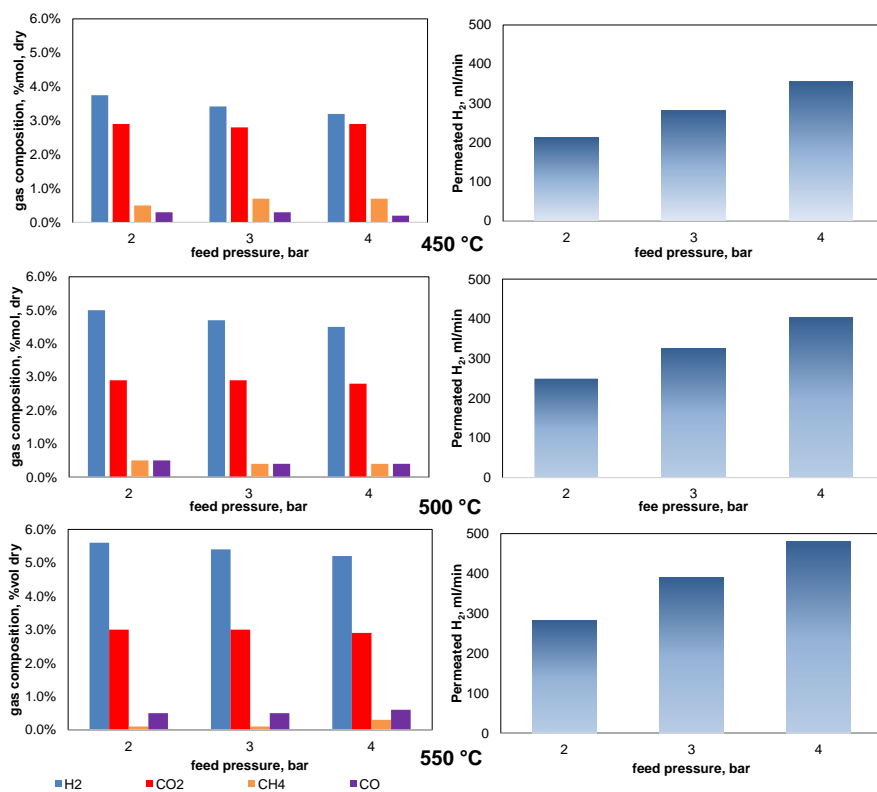


Figure 9: Results of permeation test at different temperature (450-550°C) and feed pressure (2-4 bar). The feed composition is EtOH 1.7%, H₂O 10.3%, Air 3.25%, N₂ to balance. The feed flow rate has been varied according to the u/u_{mf}

Decreasing the O₂/EtOH ratio from 0.4 to 0.2 (at 550 °C and 4 bar of feed pressure), the amount of H₂ permeated increases by 6% (from 479 to 509 Nml·min⁻¹ of H₂); however, this change does not correspond to an increase in the HRF since the amount of EtOH that react with O₂ is not considered (overall HRF equal to 45.7%). When the system is operated only for the ESR, and thus no oxygen is fed to the system, the permeated H₂ increases up to 542 Nml·min⁻¹ (+13%). This behavior can be observed in Figure 10.

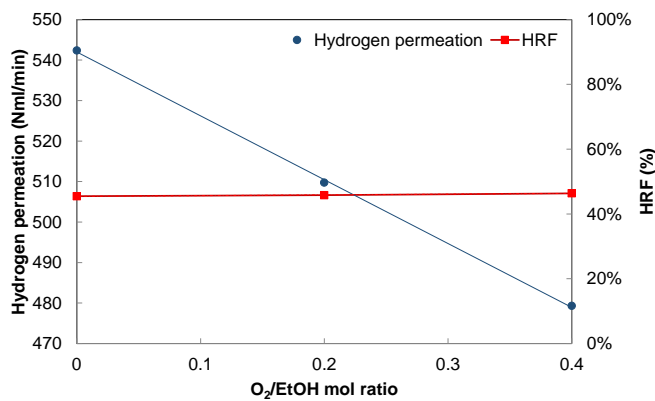


Figure 10: Effect of the O₂/EtOH ratio on the amount of hydrogen permeated and the hydrogen recovery factor in the EAR membrane reactor

A decrease in the H₂O/EtOH ratio results in a lower H₂ separation (-56%) and consequently in a lower HRF (18.1% vs 46%). As a consequence, the CO and CH₄ content in the retentate stream is increased at the expense of H₂ and CO₂.

A decrease in the u/u_{mf} from 3 to 1.5 results in an increase of the HRF (up to 85%). Despite the amount of gas at the feed side is 50% lower (with the same composition), the amount of permeated H₂ drops from 8% (at O₂/EtOH = 0.4) to 20% (at O₂/EtOH = 0). This demonstrates that in the presence of a larger membrane area, a larger H₂ flow rate can be separated at the permeate side. The experimental campaign had to be stopped after 3 weeks because of a failure in the sealing of four of the membranes.

Validation of the model

The experimental results were also used for the validation of the reactor model. For the current system, the optimum numbers of CSTRs in series for the emulsion and bubble phases were found to be 6 and 18 respectively. The same number of CSTRs were used also in Gallucci et al. [35] confirming the consistence of the model at a similar fluidization regime. Note that this implies that the bubble phase is indeed in plug flow, and that also the extent of gas back-mixing in the emulsion phase is rather small thanks to the compartmentalization via the vertically immersed membrane tube bank.

A comparison of the modeling and experimental results is shown in Figure 11. The comparison of the retentate composition (at dry and N₂-free conditions) shows a very good agreement between the model and the experimental results, as well as the comparison of the amount of permeated H₂. Additionally, all the experiments described above have been plotted in one single parity plot, in which every gas component is highlighted separately in [Figure 12](#). The

CH₄ and CO results have a somewhat larger error, above 10% (see Figure 12), which is related due to the relatively high read-off error for these components with the Sick™-analyzer. From the parity plot it can be concluded that the model with the proposed reaction kinetics, proposed reaction route, and hydrodynamics adequately describes the experimental findings.

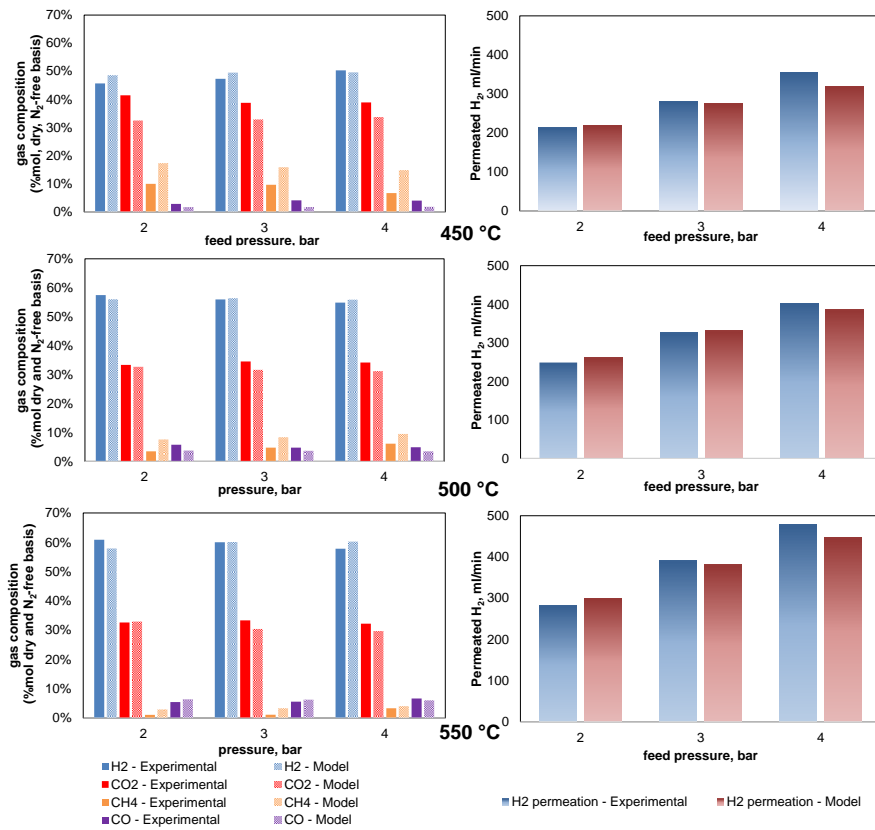


Figure 11: Comparison of experimental results and model predictions for three different temperatures. Left: retentate composition; right: permeated H₂. The retentate composition is considered after normalization at dry conditions and after removing the amount of N₂.

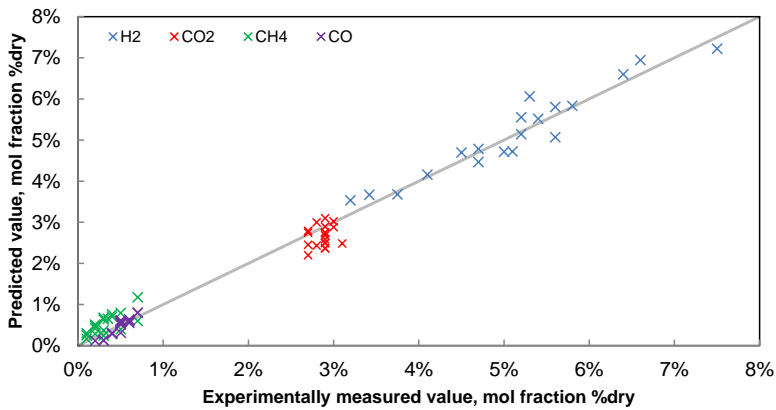


Figure 12: Parity plot of the results (modelling vs experiments)

Based on the validated model, some analysis has been carried out to compare the effect of kinetics and mass transfer on the final gas conversion at the retentate side and the H₂ production rate. From the computed axial gas composition profiles (Figure 13), one can conclude that the CO and H₂ mole fractions in the bubble and emulsion phases are very similar. The CH₄ gas fraction differs somewhat more, where the concentration in the bubble phase is higher than in the emulsion phase. This can be explained by the higher methane conversion rate by the SMR in the emulsion phase than the CH₄ mass transfer rate from the emulsion to the bubble phase (viz. $0.11 \cdot 10^{-5}$ vs. $0.78 \cdot 10^{-6}$ mol·s⁻¹), in particular at the end of the reactor because of the increased bubble size.

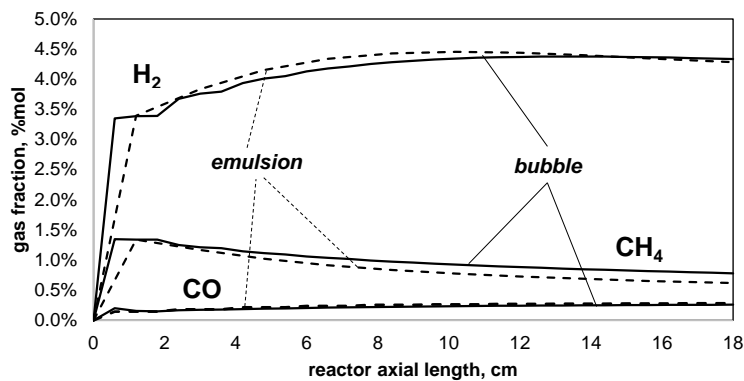


Figure 13: Axial gas composition profiles (at $T = 500$ °C, $p_{feed} = 4$ bar) for the emulsion and bubble phases

After the experimental campaign (approximately 50 hours with EtOH, three weeks under H₂/N₂ environment), the membranes were taken out of the reactor and placed in an ethanol solution

to perform helium leak test experiments (Figure 14). One membrane was broken during the shutdown, two of the membranes were leaking mostly from the bottom sealing, while the remaining two membranes were damaged at the upper sealing. This confirms that the sealing of the ceramic-supported membranes is one of the major concerns in this technology that needs to be further developed. Specifically the following recommendations can be made: 1) use of a Swagelok connection with a larger internal diameter (e.g. 12 mm instead of 10 mm); 2) use of predefined graphite ferrules that could avoid the need of any thermal or mechanical pre-treatment, so that no parts of the membrane are in direct contact with the Swagelok where usually the membrane breaks. This also requires an even better accuracy control of the shape of the ceramic supports.



Figure 14: Leakages from the sealing of the membrane after reactive test during a He leak test

The catalyst particle size distribution was also measured after the experiments and the results indicate that the averaged particle diameter has not changed ($d_{p,av} \approx 190 \mu\text{m}$). However, smaller particles ($d_p < 50 \mu\text{m}$) present in the fresh catalyst were absent. These particles have been blown out of the reactor during the experiments, since the filter to remove particles from the retentate side had to be unblocked a few times.

Design of FBMR for μCHP unit

The FluidCELL project will demonstrate the feasibility of a FBMR using EtOH as feedstock integrated with a PEM fuel cell up to 5 kW_{el} . This unit is expected to be used for domestic applications to supply electricity and heat. The FBMR is assumed to be operated at $550 \text{ }^\circ\text{C}$,

12 bar, 1 bar at the permeate side using H₂O as sweep gas ($H_2O_{sw}/H_{2,p} = 3.7 \text{ kg}_{H_2O}/\text{kg}_{H_2}$), with at the feed/retentate side a H₂O/EtOH ratio of 3.8 and an(vol.), O₂/EtOH ratio of 0.4(%vol); The resulting feeding gas mass flow rate is 6.87 kg/h and the composition as calculated from previous work [14] is EtOH 14.9%, H₂O 56.7%, O₂ 5.6%, N₂ 22.5% (molar basis).

As discussed before, the H₂ content affects the H₂ permeation rate because of the prevailing concentration polarization. Based on the permeation tests a different pre-exponential factor ($P_{H_2,0}$) has been adopted in this analysis (Eq. 28).

$$J_{H_2} = P_{H_2,0} \exp\left(-\frac{E_{H_2,p}}{RT}\right) \left(p_{H_2,r}^{0.5} - p_{H_2,p}^{0.5}\right) \quad \begin{array}{l} E_{H_2,p} = 4.57 \text{ kJ/mol} \\ P_{H_2,0} = 1.03 \cdot 10^{-3} \text{ mol/(s m}^2 \text{ Pa}^{0.5}) \end{array} \quad (28)$$

Since both the kinetics and mass transfer rates do not give rise to any limitation, the membrane area required to separate 3.2 Nm³/h of H₂ is estimated at 0.44 m². Based on this reactor design, the minimum amount of catalyst needed to keep the retentate at its thermodynamic equilibrium has been calculated. The modelling shows that for a total amount of 7 kg of solid material required to fill the reactor, about 250 g of catalyst is sufficient to achieve the required conversion. In terms of fluidization variables, the minimum u/u_{mf} is ranging from 6 to 9: at the beginning the volumetric flow rate increases because H₂ is produced while consuming CH₄; in the second part of the reactor, the u/u_{mf} decreases because of the larger H₂ permeation rate in comparison with the CH₄ conversion. The computed gas profiles at the feed/retentate are shown in Figure 15 and the amount of H₂ permeating through the membranes is reported in Figure 16.

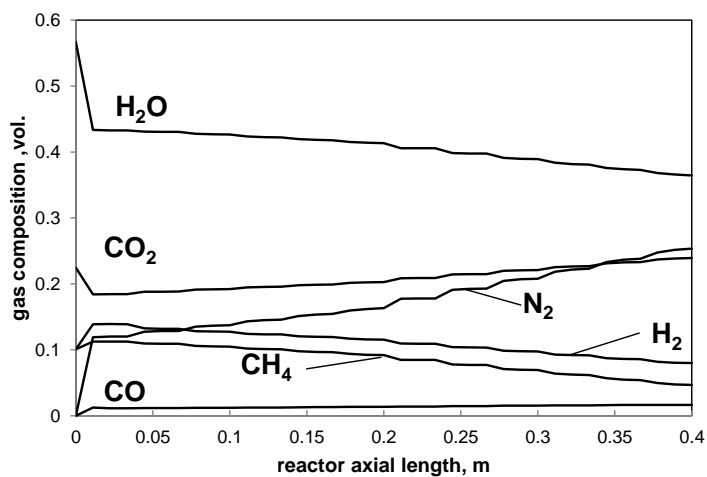


Figure 15: Axial gas composition profiles at the feed/retentate side

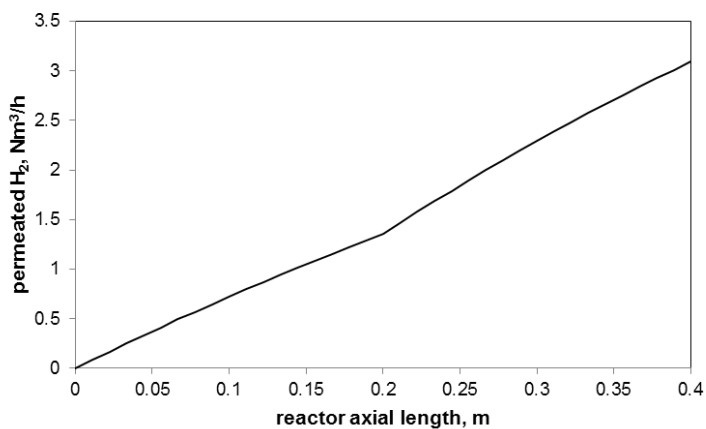


Figure 16: Volumetric flow rate of H₂ permeated along the reactor length

Conclusions

The current work has provided an experimental demonstration of a membrane reactor for ethanol auto-thermal reforming together with the validation of a phenomenological model to predict the reactor performance. The integration of EtOH conversion and H₂ separation via thin film Pd-based ceramic supported membranes has been studied and presented. The results of the permeation tests have shown a considerable influence of concentration

polarization for the empty, packed and fluidized bed configurations. The three different configurations did not show significant differences in the permeation rate, because the radial diffusion/dispersion rates were comparable for the three considered cases. The permeation tests under reactive conditions have been carried out for more than 50 hours (at reactive conditions) and in total 3 weeks under high temperature and fluidization conditions with H₂/N₂, reaching a HRF ranging from 30 to 70% (close to industrial application). The Pt-Ni based catalyst supported on a mixed CeO₂/SiO₂ has demonstrated a high activity and stability for the EAR confirming previous results. The two-phase phenomenological model of a fluidized bed membrane reactor has been described and all its parts including hydrodynamics, mass transfer, kinetics and permeation models were discussed. The validation of the model has been carried out and the model has been subsequently used for the design of a membrane reactor for μ CHP applications. For such a configuration 0.44 m² of the thin-film supported Pd-based membranes are needed to separate 3.2 Nm³·h_{H₂}⁻¹ using H₂O as sweep gas resulting in an overall HRF of 67% with a substantial reduction in the amount of required catalyst in the fluidized bed (<3.5% wt. basis). These results will be considered for the economic analysis of the system in a future work.

Acknowledgements

The presented work is funded within the FluidCELL project as part of the European Union's Seventh Framework Programme (FP7/2007-2013) for the Fuel Cells and Hydrogen Joint Technology Initiative under grant agreement n° 621196.

Nomenclature

ESR	Ethanol Steam Reforming
EAR	Ethanol Auto-Thermal Reforming
WGS	Water Gas Shift
PSA	Pressure Swing Adsorption
CHP	Combined Heat and Power
CEM	Controlled Evaporator Mixer
CSTR	Continuously Stirred Tank Reactor
FBMR	Fluidized Bed Membrane Reactor
HRF	Hydrogen Recovery Factor
PEM	Proton Exchange Membrane
PFR	Plug Flow Reactor
SMR	Steam Methane Reforming

Symbols

Ar	Archimedes Number	[-]
C _i	Concentration of component i	[mol m ⁻³]
C ₁ , C ₂	Coefficient for the bed height expansion	[-]
D _i	Diffusion coefficient of component i	[m ² s ⁻¹]
d _b	Bubble diameter	[m]

d_p	Particle diameter	[m]
d_t	Tube diameter	[m]
E_a	Activation energy	[kJ mol ⁻¹]
g	Gravity constant	[m s ⁻²]
H	Bed height	[m]
J	Partial flux	[mol s ⁻¹]
K_{eq}	Equilibrium constant	[-]
K_{bc}, K_{bc}, K_{ce}	Gas exchange coefficients (bubble –cloud-emulsion phase)	[s ⁻¹]
k_i	Forward reaction rate constant for reaction i	[mol kg _{cat} ⁻¹ s ⁻¹ Pa ⁻²]
$P_{H_2,0}$	Permeability of Pd-Ag membrane to H ₂	[mol s ⁻¹ m ⁻¹ Pa ⁻ⁿ]
p_i	Partial pressure of component i	[Pa] or [bar]
R	Gas constant	[J mol ⁻¹ K ⁻¹]
Re	Reynolds number	[-]
Re_{mf}	Reynolds number at minimum fluidization	[-]
r_x	Reaction rate of reaction x	[mol s ⁻¹]
M_i	Molecular weight component i	[g mol ⁻¹]
S	Selectivity	[-]
T	Temperature	[K]
u_g	Gas velocity	[m s ⁻¹]
u_{mf}	Minimum fluidization velocity	[m s ⁻¹]
y_i	Molar fraction of component i in gas phase	[-]
ϕ	Sphericity	[-]
δ	Bubble/emulsion phase fraction	[-]
ε	Porosity	[-]
ε_{mf}	Porosity at minimum fluidization velocity	[-]
μ_i	Viscosity of component i	[kg s ⁻¹ m ⁻¹]
ρ_i	Gas/particle Density	[kg m ⁻³]
K_{ij}	i-phase to j-phase gas exchange coefficient	[s ⁻¹]

Commentato [M.1]: Also include all the symbols in the equations in the tables... Then many are missing...

References

- [1] K. Wawrzinek, C. Keller, FunchHy-Workshop (2007).
- [2] S. Dunn, Int. J. Hydrogen Energy 27 (2002) 235.
- [3] T. Rostrup-Nielsen, Catal. Today 106 (2005) 293.
- [4] IEA, Technology Roadmap Hydrogen and Fuel Cells, 2015.
- [5] M. Ni, D.Y.C. Leung, M.K.H. Leung, Int. J. Hydrogen Energy 32 (2007) 3238.
- [6] G. a Deluga, J.R. Salge, L.D. Schmidt, X.E. Verykios, Science (80-.). 303 (2004) 993.
- [7] Renewable Fuel Association, 2016 Ethanol Industry Outlook, 2016.
- [8] P.H. Pfromm, V. Amanor-Boadu, R. Nelson, P. Vadlani, R. Madl, Biomass and Bioenergy 34 (2010) 515.
- [9] T. Hou, S. Zhang, Y. Chen, D. Wang, W. Cai, Renew. Sustain. Energy Rev. 44 (2015) 132.
- [10] A. Haryanto, S. Fernando, N. Murali, S. Adhikari, Energy & Fuels (2005) 2098.
- [11] V. Palma, F. Castaldo, P. Ciambelli, G. Iaquaniello, Appl. Catal. B Environ. 145 (2014) 73.
- [12] C. Ruocco, E. Meloni, V. Palma, M. van Sint Annaland, V. Spallina, F. Gallucci, Int. J. Hydrogen Energy 41 (2016) 20122.
- [13] V. Palma, C. Ruocco, E. Meloni, A. Ricca, Int. J. Hydrogen Energy 42 (2016) 1598.
- [14] S. Foresti, G. Manzolini, Int. J. Hydrogen Energy 41 (2016) 9004.
- [15] C. Galletti, S. Specchia, G. Saracco, V. Specchia, Chem. Eng. Sci. 65 (2010) 590.
- [16] A. Basile, F. Gallucci, A. Iulianelli, S. Tosti, Fuel Cells 8 (2008) 62.
- [17] F. Gallucci, M. Van Sint Annaland, J.A.M. Kuipers, Int. J. Hydrogen Energy 35 (2010) 1659.
- [18] F. Borgognoni, S. Tosti, M. Vadrucchi, A. Santucci, Int. J. Hydrogen Energy 38 (2013) 1430.

- [19] E. Fernandez, J.A. Sanchez-Garcia, J. Melendez, V. Spallina, M. van Sint Annaland, F. Gallucci, D.A. Pacheco Tanaka, *Chem. Eng. J.* 305 (2016) 149.
- [20] E. Acha, J. Requies, V.L. Barrio, J.F. Cambra, M.B. Güemez, P.L. Arias, Y.C. van Delft, *J. Memb. Sci.* 415–416 (2012) 66.
- [21] M. Sarić, Y.C. Van Delft, R. Sumbharaju, D.F. Meyer, A. De Groot, *Catal. Today* 193 (2012) 74.
- [22] N. Vicinanza, I.H. Svenum, L.N. Næss, T.A. Peters, R. Bredesen, A. Borg, H.J. Venvik, *J. Memb. Sci.* 476 (2015) 602.
- [23] J.A. Medrano, E. Fernandez, J. Melendez, M. Parco, D.A.P. Tanaka, M. Van Sint Annaland, F. Gallucci, *Int. J. Hydrogen Energy* 41 (2016) 8706.
- [24] A. Helmi, E. Fernandez, J. Melendez, D.A.P. Tanaka, F. Gallucci, M. Van Sint Annaland, *Molecules* 21 (2016).
- [25] A. Brunetti, A. Caravella, E. Fernandez, D.A. Pacheco Tanaka, F. Gallucci, E. Drioli, E. Curcio, J.L. Viviente, G. Barbieri, *Int. J. Hydrogen Energy* 40 (2015) 10883.
- [26] M. De Falco, *Fuel* 90 (2011) 739.
- [27] A. Arratibel Plazaola, D. Pacheco Tanaka, M. Van Sint Annaland, F. Gallucci, *Molecules* 22 (2017) 51.
- [28] S. Maurer, E.C. Wagner, T.J. Schildhauer, J.R. van Ommen, S.M.A. Biollaz, R.F. Mudde, *Int. J. Multiph. Flow* 74 (2015) 118.
- [29] T.Y.N. Dang, F. Gallucci, M. Van Sint Annaland, *Chem. Eng. Sci.* 108 (2014) 194.
- [30] N.T.Y. Dang, F. Gallucci, M. Van Sint Annaland, *Chem. Eng. J.* 239 (2014) 42.
- [31] D.A. Pacheco Tanaka, M.A. Llosa Tanco, S.I. Niwa, Y. Wakui, F. Mizukami, T. Namba, T.M. Suzuki, *J. Memb. Sci.* 247 (2005) 21.
- [32] W. Chen, X. Hu, R. Wang, Y. Huang, *Sep. Purif. Technol.* 72 (2010) 92.
- [33] E. Fernandez, K. Coenen, A. Helmi, J. Melendez, J. Zuñiga, D.A. Pacheco Tanaka, M. Van Sint Annaland, F. Gallucci, *Int. J. Hydrogen Energy* 40 (2015) 13463.
- [34] F. Gallucci, M. van Sint Annaland, J. Kuipers, *Top. Catal.* 51 (2008) 133.
- [35] F. Gallucci, M. van Sint Annaland, J. Kuipers, *Top. Catal.* 51 (2008) 146.
- [36] D. Kunii, O. Levenspiel, *Fluidization Engineering*, Elsevier, 1991.
- [37] C.-Y. Shiau, C.-J. Lin, *AIChE J.* 37 (1991) 953.
- [38] S. Mori, C.Y. Wen, *AIChE J.* 21 (1975) 109.
- [39] O. Carmody, R. Frost, Y. Xi, S. Kokot, *Surf. Sci.* 601 (2007) 2066.
- [40] [P. Schneider, *Appl. Cat. A: Gen.* 129 \(1995\) 157-165.](#)
- [41] S. Kang, B. Sub Kwak, M. Kang, *Ceram. Int.* 40 (2014) 14197.
- [42] V. Palma, C. Ruocco, A. Ricca, *Int. J. Hydrogen Energy* 41 (2016) 11526.
- [43] [V. Palma, C. Ruocco, E. Meloni, A. Ricca, *J. Cle. Prod.* 166 \(2017\) 263-272.](#)
- [44] [D. Li, K. Nishida, Y. Zhan, T. Shishido, Y. Oumi, T. Sano, K. Takehira, *App. Cat. A: Gen.* 350 \(2008\) 225-236.](#)
- [45] A.G.M. da Silva, H. V. Fajardo, R. Balzer, L.F.D. Probst, N.T. Prado, P.H.C. Camargo, P.A. Robles-Dutenhefner, *Chem. Eng. J.* 286 (2016) 369.
- [46] J. Zhang, D. Liu, M. He, H. Xu, W. Li, *J. Memb. Sci.* 274 (2006) 83.
- [47] T. Nakajima, T. Kume, Y. Ikeda, M. Shiraki, H. Kurokawa, T. Iseki, M. Kajitani, H. Tanaka, H. Hikosaka, Y. Takagi, M. Ito, *Int. J. Hydrogen Energy* 40 (2015) 11451.
- [48] S. Hara, K. Sakaki, N. Itoh, *Ind. Eng. Chem. Res.* 38 (1999) 4913.
- [49] A. Caravella, L. Melone, Y. Sun, A. Brunetti, E. Drioli, G. Barbieri, *Int. J. Hydrogen Energy* 41 (2016) 2660.
- [50] E. Fernandez, A. Helmi, K. Coenen, J. Melendez, J.L. Viviente, D.A. Pacheco Tanaka, M. van Sint Annaland, F. Gallucci, *Int. J. Hydrogen Energy* 40 (2015) 3506.

Formattato: Inglese (Stati Uniti)

[49] E. Tsotsas, E.U. Schlünder, Chem. Eng. Sci. 45 (1990) 819.

Commentato [M.2]: Check the names!!!